

SCIENTIFIC REPORTS

OPEN

Pan-Renal Cell Carcinoma classification and survival prediction from histopathology images using deep learning

Sairam Tabibu¹, P. K. Vinod² & C. V. Jawahar¹

Received: 28 February 2019
Accepted: 28 June 2019
Published online: 19 July 2019

Histopathological images contain morphological markers of disease progression that have diagnostic and predictive values. In this study, we demonstrate how deep learning framework can be used for an automatic classification of Renal Cell Carcinoma (RCC) subtypes, and for identification of features that predict survival outcome from digital histopathological images. Convolutional neural networks (CNN's) trained on whole-slide images distinguish clear cell and chromophobe RCC from normal tissue with a classification accuracy of 93.39% and 87.34%, respectively. Further, a CNN trained to distinguish clear cell, chromophobe and papillary RCC achieves a classification accuracy of 94.07%. Here, we introduced a novel support vector machine-based method that helped to break the multi-class classification task into multiple binary classification tasks which not only improved the performance of the model but also helped to deal with data imbalance. Finally, we extracted the morphological features from high probability tumor regions identified by the CNN to predict patient survival outcome of most common clear cell RCC. The generated risk index based on both tumor shape and nuclei features are significantly associated with patient survival outcome. These results highlight that deep learning can play a role in both cancer diagnosis and prognosis.

Kidney Cancer accounts for nearly 3.8% of adult cancers and is among the 10 most common cancers in both men and women. Recent estimate by American Cancer Society indicates that 63340 new cases and 14970 death will occur in 2018¹. Renal Cell Carcinoma (RCC) is the most common (85%) malignant tumor of kidney and is a heterogeneous group of tumors with different histology, molecular characteristics, clinical outcomes and responses to therapy². The major subtypes of RCC are clear cell, papillary and chromophobe accounting for 70–80%, 14–17% and 4–8% of RCC, respectively^{3,4}.

Clear cell RCC (KIRC) and papillary RCC (KIRP) originate from cells in the proximal convoluted tubules of the nephron⁵. KIRC is characterized with loss of chromosome 3p and mutation of the von Hippel–Lindau (VHL) gene while KIRP is characterized by trisomy of chromosomes and loss of chromosome 9p^{6,7}. Chromophobe RCC (KICH) originates from intercalated cells in the distal convoluted tubules and is characterized by loss of chromosomes⁸. KIRC patients have an overall 5-year survival rate of 55–60%^{9–11} whereas for KIRP patients, it varies from 80–90%^{12,13} and for KICH patients, it is 90%¹⁴. Due to these distinct biological and clinical behavior of subtypes, accurate detection of RCC and its subtypes is vital for the clinical management of patients.

RCC subtypes can be detected radiologically based on degree of tumor enhancement on multidetector computed tomography (CT) or magnetic resonance imaging (MRI)^{15–19}. Further, the microscopic examination of Hematoxylin and Eosin (H & E) stained slides of biopsies continues to be a valuable tool for pathologist and clinicians²⁰. Histological images contain markers of disease progression and phenotypic information that can have diagnostic and predictive values. Most pathologists follow simple decision tree-based approaches for tumor stratification. Major limitations in the examination of H & E images by pathologists are inter-observer discordance and time required to diagnose. Computer-aided approaches can help to overcome these limitations and to identify subtle morphological differences between clinical groups.

¹Center for Visual Information Technology, IIIT, Hyderabad, India. ²Center for Computational Natural Sciences and Bioinformatics, IIIT Hyderabad, Hyderabad, India. Correspondence and requests for materials should be addressed to S.T. (email: t.sairam.ece13@iitbhu.ac.in) or P.K.V. (email: vinod.pk@iiit.ac.in) or C.V.J. (email: jawahar@iiit.ac.in)

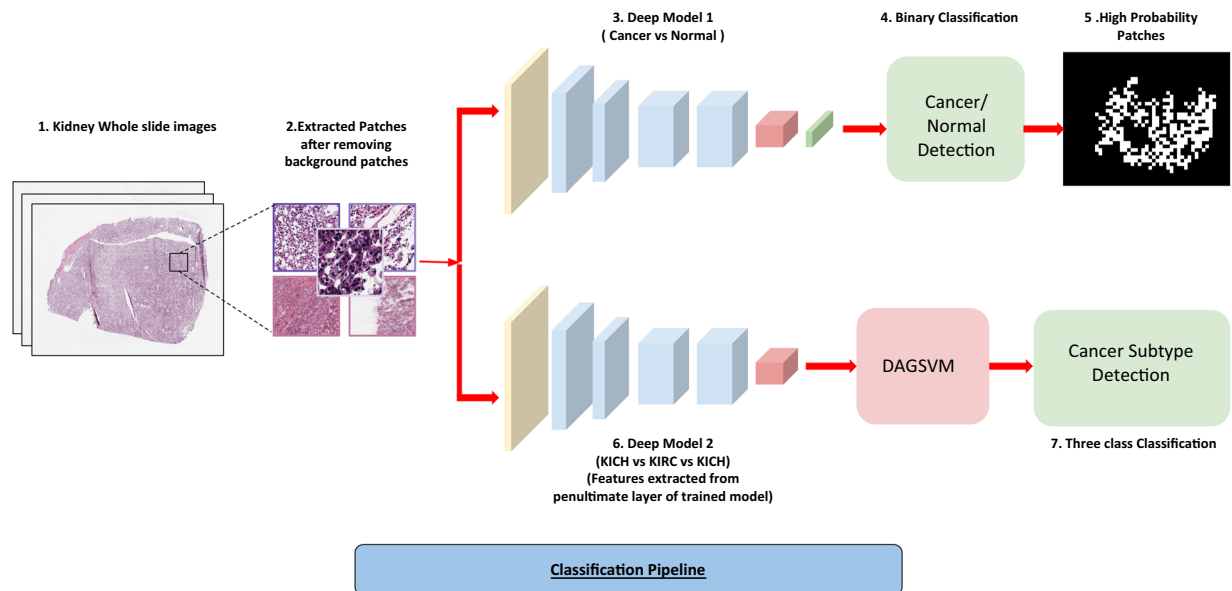


Figure 1. Cancer Classification Pipeline. (1) Kidney Whole slide images. (2) 512*512 patches extracted from images with 50% overlap and background removed using pixel thresholding. (3) Patches from normal and cancerous slides fed to the deep network. (4) Patches classified as cancerous or non-cancerous. (5) High probability patches identified by the trained network and binary mask is applied. (6) The patches from three subtypes used to train a similar deep architecture for a three-way classification. (7) Features extracted from the penultimate layer of the network and fed to DAG-SVM and a three-way classification is performed by it.

The Cancer Genome Atlas (TCGA)^{21,22} project has resulted in the creation of large repositories of digital H & E whole-slide images (WSI) of RCC. These images are acquired at 20x and 40x magnifications with size varying from 10000–100000 pixels, which are visually tricky to analyze and interpret accurately. Further, the high-resolution WSI also poses a challenge to develop computational model for classification. An automated system to detect RCC and its subtypes is still not available. Cheng *et al.*²³ extracted image features from TCGA tumor slides to develop a lasso-regularized Cox model for predicting survival of KIRC patients.

In recent years, deep learning techniques especially convolutional neural networks (CNN's) have significantly improved accuracy on a wide range of computer vision tasks such as image recognition^{24–26}, object detection^{27,28} and semantic segmentation^{27,29}. Further, CNN's have also been successful in capturing the complex tissue patterns and have been widely used in biomedical imaging for segmentation as well as for classification tasks in cancers such as breast^{30–32}, lung^{33–36} and prostate³⁷.

In this study, we demonstrate how deep learning can be applied to histopathological images of RCC. An automatic system for pan-RCC classification and survival prediction tasks was developed from WSI of TCGA. CNN's trained on WSI classify each RCC subtype from normal tissues and three RCC subtypes, and extract features for survival prediction. In that process, we also characterized the high probability cancerous regions and tissue of origin differences and came up with a strategy for overcoming data imbalance in multi-class classification problems using histopathological images.

Results

CNN model to distinguish RCC from normal tissue using histopathology images. TCGA slide images of RCC and normal tissues were split into 70-15-15% for training, validation and testing (Supplementary Tables 1–3). Image patches of size 512 × 512 were extracted from the slides of both 20x and 40x resolution with 50% overlap (Fig. 1). The background patches were removed using pixel thresholding (See Methods Section). We used the pre-trained Resnet 18 and Resnet 34 by replacing the last layers with just 2 output layers and fine-tuned it on RCC data. We terminated the training after 30 epochs when the validation accuracy failed to improve. The images were processed patch-wise as well as slide-wise. We trained the model on only KIRC and KICH due to lack of sufficient normal tissue samples for KIRP. We obtained 93.39% and 87.34% (Tables 1 and 2) patch-wise accuracy on the test set for KIRC and KICH, respectively. To assess this accuracy, we performed a slide-wise analysis by counting the percentage of positively classified patches in a slide. We achieved a best Area Under Curve (AUC) of 0.98 for KIRC and 0.95 for KICH using Resnet 34 (Table 2).

RCC subtype detection using CNN. A challenging task is to distinguish the subtypes of RCC: KIRC, KIRP and KICH. We used the deep learning framework to distinguish these three subtypes (Fig. 1). However, there exists a major class imbalance with 43% KIRC, 14% KIRP and 43% KICH images. First, we tested whether the CNN can distinguish these subtypes irrespective of the data imbalance. We extracted the 512 × 512 patches from 20x resolution for each subtype and performed a three-class classification using Resnet-18 and Resnet-34. We obtained a patch-wise accuracy of 87.69% and a micro-average AUC of 0.91 with Kappa score of 0.794 (Table 3).

| Model | Patch-wise Accuracy | Precision | Recall | Slide-wise AUC |
|------------------|---------------------|-----------|--------|----------------|
| Resnet-18 (KIRC) | 90.20 | 90.23 | 88.35 | 0.97 |
| Resnet-34 (KIRC) | 89.22 | 89.61 | 86.84 | 0.98 |
| Resnet-18 (KICH) | 84.68 | 85.78 | 82.92 | 0.92 |
| Resnet-34 (KICH) | 87.34 | 87.57 | 86.34 | 0.98 |

Table 1. Cancer/Normal Classification (20x resolution).

| Model | Patch-wise Accuracy | Precision | Recall | Slide-wise AUC |
|------------------|---------------------|-----------|--------|----------------|
| Resnet-18 (KIRC) | 93.39 | 93.41 | 92.95 | 0.99 |
| Resnet-34 (KIRC) | 93.62 | 93.47 | 93.37 | 0.99 |
| Resnet-18 (KICH) | 79.09 | 79.61 | 80.06 | 0.95 |
| Resnet-34 (KICH) | 80.57 | 80.65 | 81.17 | 0.95 |

Table 2. Cancer/Normal Classification (40x resolution).

| Model | Patch-wise Accuracy | Precision | Recall | Slide-wise AUC |
|---------------------|---------------------|-----------|--------|----------------|
| Resnet-18 | 87.69 | 88.82 | 83.66 | 0.88 |
| Resnet-34 | 86.19 | 88.30 | 83.18 | 0.88 |
| Resnet-18 + DAG-SVM | 92.62 | 90.78 | 89.07 | 0.93 |
| Resnet-34 + DAG-SVM | 91.96 | 88.94 | 87.92 | 0.93 |

Table 3. Cancer subtype classification.

However, the recall score is in the range of 83% suggesting that certain classes are misclassified. Individual analysis of the classification scores on each subtype (Supplementary Table 4) revealed that the CNN performs better on subtypes KIRC and KICH but not on KIRP (70%) which can be attributed to the severe data imbalance within the subtypes.

We used a DAG-SVM method³⁸ to deal with this data imbalance method without making any changes to the deep learning architecture. In this framework, the N-class classification problem is divided into $N(N-1)/2$ binary classification problem by replacing the softmax layer of deep architecture by binary classifiers for each pair of classes arranged in a directed acyclic graph (DAG) structure (Fig. 2). Such division enables the network to focus on individual binary problems which are relatively easier to tackle as well as to learn more pairwise discriminative features (See Methods Section). Using the representation matrix obtained by the CNN from the penultimate layer of the CNN for patch images, we trained the DAG-SVM and performed the subtype classification. We obtained a substantial increase in the patch-wise accuracy by 5% (Table 3). The increase in the micro-average AUC is 0.03 whereas macro-average AUC is 0.05. This demonstrates that the combined CNN and DAG-SVM model substantially improves the performance of discriminating the subtypes even in the given limitation of data imbalance. This is also evident from the increase in the classification score of the subtype KIRP (10%) (Supplementary Table 5).

Further, we also applied two alternative strategies to overcome the class imbalance problem. First, data augmentation of the minority class was done to balance the class distribution. We obtained an accuracy of 91.47% with a Kappa score of 0.859. Second, a weighted resampling technique was used to train the CNN such that the minority class gets more weightage depending on the severity of the imbalance. We obtained an accuracy of 92.16% with a Kappa score of 0.871. Both these methods significantly improved the subtype classification accuracy (Supplementary Table 6). Furthermore, we applied DAG-SVM to both the data augmentation and sampled models and observed an increase in accuracy by 2.28% in case of augmented model and 2.35% in case of sampled model.

Prediction of tumor areas and the survival outcome for KIRC. Using the CNN model that distinguishes RCC from normal tissue, high probability tumor patches were identified, and a probability heat map was generated for the WSI. Based on the tumor region, several tumor and nuclei shape features such as area, perimeter etc. were extracted from the cancer slide images of each patient (Fig. 3). The risk index of each patients was calculated using lasso-regularized COX model for each feature and validated using two-level cross validation strategy (see methods).

Figure 4 shows the survival curves of low and high-risk groups for different features. We found that 13 tumor shape features and 6 nuclei shape features are significantly (p value less than 0.05) associated with the patient survival (Table 4). Tumor shape features include total area (p value = $1.5e-6$, HR = 2.398) and total perimeter (p value = $1.49e-5$, HR = 2.485), and nuclei shape features include total convex area (p value = $2.2e-7$, HR = 2.576) and total major axis (p = 0.000614, HR = 2.252) (Fig. 4A–C). Most predictive individual features were selected

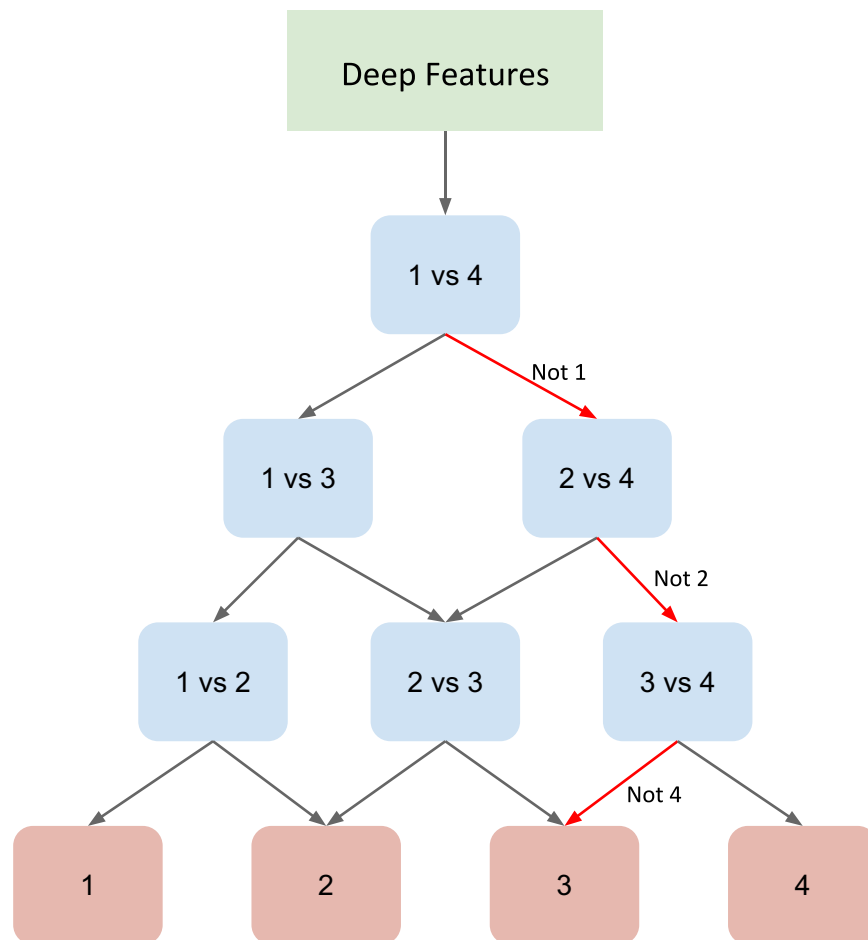


Figure 2. Directed Acyclic Graph SVM (DAG-SVM)-Architecture of the model for a four-class problem where features learned by the deep network are used to train all the classifiers. Each node is a binary classifier for a pair of classes.

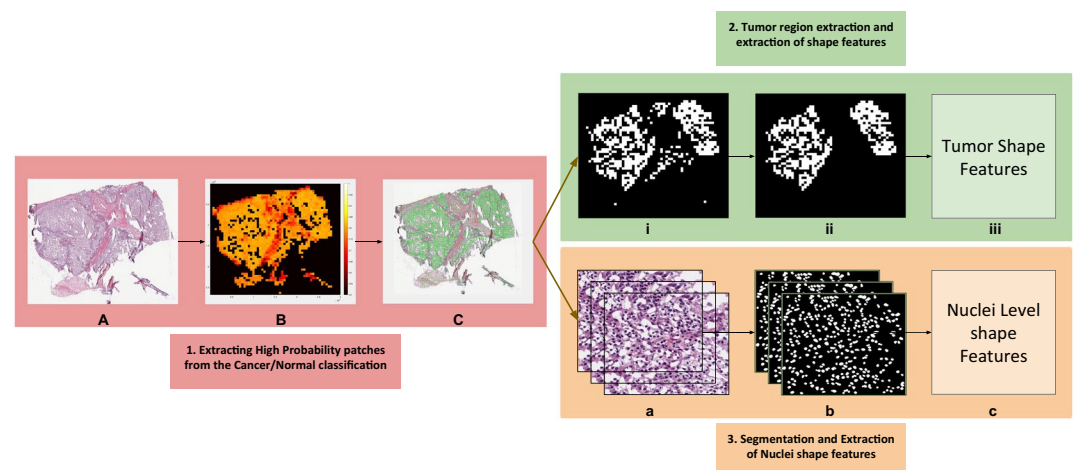


Figure 3. Shape Features Extraction Pipeline. (A) Tissue slide image. (B) Heatmap generated after each patch is fed through the deep network. (C) High probability patches are highlighted. (i) Binary mask generated for high probability patches. (ii) Small patches removed using morphological operations. (iii) Tumor shape features extracted from final image. (a) High probability patches accumulated. (b) Nuclei segmented from each patch. (c) Nuclei shape features extracted from each patch.

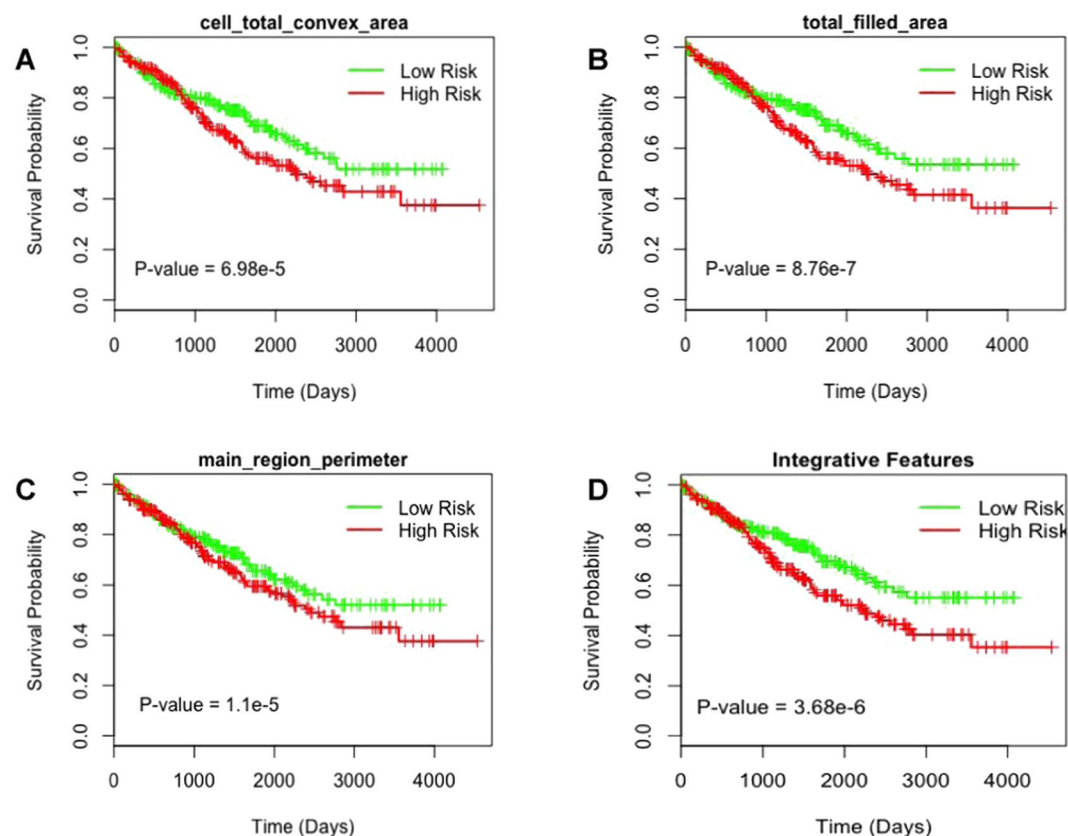


Figure 4. Tumor shape and cell shape features predict survival outcome of KIRC patients.

| Feature type | Image feature | p-value |
|-----------------------|-------------------------------|----------|
| Tumor shape features | Total area | 1.5e-6 |
| | Total convex area | 2.2e-7 |
| | Total perimeter | 1.49e-5 |
| | Total filled area | 8.76e-7 |
| | Total major Axis | 0.000614 |
| | Total minor axis | 0.000572 |
| | Total perimeter by Area | 0.00139 |
| | Main region area | 0.0042 |
| | Main region convex area | 1.58e-5 |
| | Main region perimeter | 1.1e-5 |
| | Main region perimeter by area | 4.29e-5 |
| | Main region major axis | 6.09e-5 |
| | Main region minor axis | 0.00161 |
| Nuclei shape features | total area | 0.000106 |
| | Total convex area | 6.98e-5 |
| | Total perimeter | 0.00327 |
| | Total filled area | 0.000115 |
| | Total major axis | 0.00251 |
| | Total minor axis | 0.00748 |
| Integrative model | | 3.68e-6 |

Table 4. Tumor shape and Nuclei features and their log-rank test p-values.

for integrative analysis to stratify patients into low risk and high-risk groups using Lasso-Cox model. We found significant (p value = $3.68e-6$) association between combined image features and survival outcome (Fig. 4D). Multivariate analysis was performed with predicted risk indices, age, gender, grade and stage as covariates (Table 5). We observed that the survival outcome significantly depends on the predicted risk indices and stages of

| Variable | HR(95% CI) | p-value |
|-----------|----------------------|----------|
| Lasso Cox | 2.265 (1.5343–3.343) | 3.87e-5 |
| Age | 1 (0.999–1.0001) | 3.71e-6 |
| Gender | 1.095 (0.7870–1.524) | 0.590 |
| Stage | 1.733 (1.4968–2.007) | 2.01e-13 |
| Grade | 1.106 (0.9369–1.306) | 0.233 |

Table 5. Multivariate analysis of predicted risk indices.

tumor. This suggest that tumor and cell nuclei shape features identified in this study can be used as a prognostic factor to predict the survival outcome of KIRC patients.

Discussion

In this study, we developed an automatic system that can distinguish RCC from normal tissue and RCC subtypes using histopathology images. To the best of our knowledge, this is the first study to perform classification of RCC subtypes using deep learning framework. CNN's successfully identified the cancerous tissue patterns as well as the inherent texture differences among RCC subtypes. We also introduced a method to deal with data imbalance which can be generalized to other cancer classification tasks. Finally, we developed a prognostic model based on the regions detected by the CNN to predict survival outcome. We used a two-level cross validation technique to validate our model.

Due to the enormous amount of information contained in the WSI, the histopathological analysis is a laborious and time intensive task for the pathologist. With the growing number of cancer cases, fast and precise assessment is not feasible. Our study addresses this limitation by providing computational interpretation of WSI with high AUCs in the testing phase of various classification tasks. Since the pipeline was developed on the WSI of cancer, it eliminates the requirement of annotating tumor regions for the training purpose and provides a strategy that can used to study WSI of other tumors. Further, a high patch-wise AUC obtained for distinguishing tumor from normal tissue suggests that tumor regions are not localized and are spread across WSI. Our analysis also showed that a better performance is obtained for KIRC when trained on 40x images and for KICH when trained on 20x images (Tables 1 and 2). These results suggest the existence of complex morphological distinguishing features between cancers.

Subtypes of RCC typically have varying morphological patterns and nuclear/cytoplasmic features at the microscopic level³⁹. Different cases of KIRC have mixture of cells with clear cytoplasm and granular eosinophilic cytoplasm, pseudopapillary pattern, rich vascularity and areas of hemorrhage. KICH has polygonal cells with prominent cell membranes, cells of different size with either eosinophilic or foamy cytoplasm and incomplete vascular septae. KIRC has predominantly papillary growth pattern, foamy macrophages and cuboidal cells. However, there are instances where histopathology images are not conclusive leading to re-classification of some KIRC samples as KICH during the histological review⁴⁰.

The CNN model is able to distinguish these subtypes by capturing their unique characteristics with high AUC of 0.93 (Table 3). Further, we also tested whether the inherent difference in the texture of tissue of origin contribute to classification of subtypes by using normal tissue samples as a test set to RCC subtype model. We obtained subtypes classification with AUC of 0.85 (Supplementary Table 7). Together, these analyses suggest that both tumor regions and the inherent texture difference contributes to subtype classification. Texture classification methods⁴¹ can be further used to visualize the difference (Fig. 5) and study their characteristics. Further, for subtype detection, we introduced a DAG-SVM classifier on the top of the deep network. This helped to break the multi-class classification task into multiple binary classification tasks which not only improved the performance of the model but also helped to deal with data imbalance. DAG-SVM is useful when the deep networks lack the scope for improvement without a major change in architecture. This method can also be applied to different deep architectures, since the method focuses only on the output layer.

Finally, we also demonstrated the reliability of features extracted from tumor slide images in predicting the survival outcome. We showed that both tumor shape and nuclei features from the high probability regions identified by CNN are significantly associated with survival outcome of KIRC. Image features such as ratio of perimeter squared by area, which is a quantification of tumor surface³⁴, is correlated with survival outcome. A major finding that tumor shape features also predict survival extends the previous studies that uses genomic and nuclei features to predict survival of KIRC. It is also consistent with observation that tumor shape features can be used to predict the survival outcome of lung patients³⁴. However, this model is developed using annotated images by pathologist, which in our case is done independent of any human bias.

The lack of data and the class imbalance are major challenges in building survival models of other subtypes. Firstly, there is dearth of KIRP-matched normal slide images that can be used to develop a model to distinguish tumor from normal tissue and to identify high probability cancerous regions. Secondly, since the ratio of events (death) to total number of patients is few for KICH and KIRP (less than 15%) compared to KIRC (around 40%), the survival prediction for KICH and KIRP is affected. Further, subtypes such as renal oncocytoma and collecting duct (Bellini duct) of RCC have the rarest chance to occur (less than 1%) and therefore data is scarce to develop model including rare subtypes. On the other hand, we made several attempts to use only tumor slide images of KIRP to classify different tumor stages and grades, which did not yield satisfactory performance. Further study in this direction is required to see whether improvements in deep learning framework can help to detect the subtle differences between early and late stages of RCC and to integrate genomic features to improve the performance.

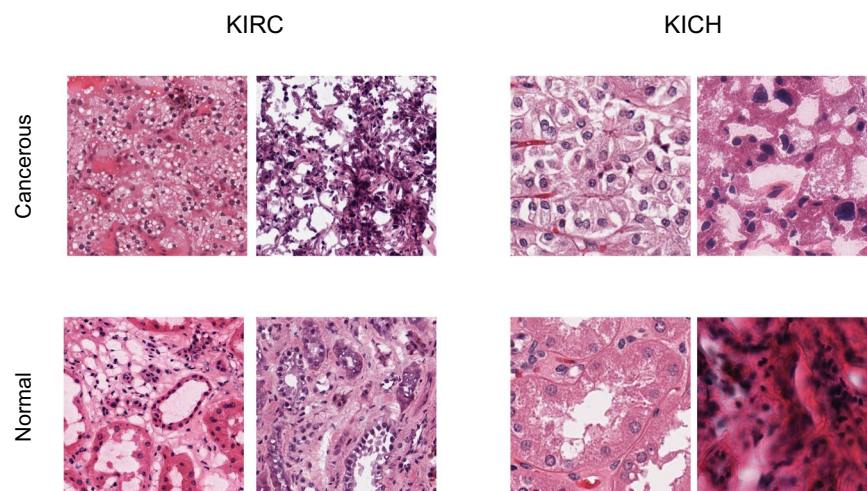


Figure 5. Visualization of cancerous and normal tissue regions at 40x resolution.

Studies to understand the complex relationship between tissue histology and genetics can provide useful insights for the diagnosis and treatment.

Methods

Dataset and image processing. The whole slide images and clinical information were downloaded from TCGA data portal (<https://gdc.cancer.gov/>). Slides with reading and compatibility issues were removed (972 slides in total were removed from the whole dataset). We selected 1027 (KIRC), 303 (KIRP), and 254 (KICH) tumor slide images for our study. Further, corresponding 379, 47 and 83 normal tissue slide images for each subtype were selected. 512*512 sized tiles were extracted with 50% overlap ensuring multiple viewpoints within the tissue, at a magnification of 20x and 40x. For subtype classification, patches from 20x magnification were used. The patches were removed if the mean intensity of 50%-pixel values was larger than a threshold (in our case 210 for RGB channels).

Training architecture and framework. The Resnet 18 and 34 architectures²⁴ pre-trained on Imagenet dataset were used with input resized from 512*512 to 224*224. The final linear layer was modified to 2 for cancer/normal detection and 3 for subtype detection. The network was fine-tuned with stochastic gradient optimizer and cross entropy was used as the loss function. To introduce generalization, we also used data augmentation techniques (random horizontal flip and random Crop) while training. The images before being fed to the network were normalized using mean and standard deviation which was calculated on the training set. Batch size was set to 128 with learning rate 1e-5 and decay according to the validation error. The average number of epochs for both experiments lies in between 3–40 epochs. The training was terminated when the validation accuracy did not vary much for 4–5 epochs. Tests were implemented using Pytorch library⁴². For the 3-class classification problem in the subtype detection, we used a DAG-SVM on the top of the fully connected layer of the CNN to improve the multiclass accuracy. We removed the final softmax layer from the trained model and use the learned representation given by the CNN (which is essentially a 512*1 vector) to train the DAG-SVM. Linear kernel was used while training the SVMs.

A two-step procedure was followed for data augmentation. First, random patches were chosen from the minority class and then three augmentation techniques: random vertical flip, rotation (−25 to +25 degrees) and adding noise to image were applied with a probability of 0.5 to the selected image. 100000 augmented images were generated using this technique from 74000 images. Further, a weighted resampling technique was also used to overcome the class imbalance. The weights were assigned according to the class distribution of the respective subtypes using the WeightedRandomSampler function in pytorch. The training parameters were kept the same.

Mapping high probability regions and survival analysis. The survival analysis was performed on KIRC WSI's (Supplementary Table 8) The probability score for each patch was calculated by passing them through the KIRC CNN model (normal/cancer) trained on patches in 40x resolution, and a heatmap was constructed for each slide (Supplementary Figs 1 and 2). The high probability regions (greater than 0.95) were highlighted using binary masking. To remove the effects of very small patches, tissue regions which were less than 1/3rd of the main region were removed. 15 shape features including region area, convex area, perimeter, solidity, and eccentricity were extracted from the high probability patches. Further, the nuclei were segmented using a hierarchical multilevel thresholding approach⁴³ and 7 nuclei shape features were extracted (Supplementary Table 9). In this approach, the parameter values are set adaptively eliminating the need for parameter learning or training data. If a patient had one or more slides the values were averaged and patient level features were aggregated. We used these morphological features to build a Lasso regularized COX model. We estimated the risk index of each patient based on each morphological feature. A two-level cross validation strategy was used to validate our model²³. Each patient was kept aside as a test case and the rest of the samples were used to train the COX model using a 10-fold

cross validation. The model was then used to stratify the left out patient into either high risk or low risk group using the median score obtained from the training set. This process was repeated until each patient was used as a test set. From the finally obtained groups and survival indices, p-values were calculated using log-rank test. We used Kaplan-Meier plots to visualize the survival curves of low and high-risk groups. The survival analysis was performed using R packages “survival” and “glmnet”^{44,45}.

Data Availability

The source code is made publicly available at <https://github.com/tabibusairam/Pan-Renal-cancer.git>.

References

1. American cancer society, <http://www.cancer.org/cancer/kidneycancer>. Accessed: 2018-10-1.
2. Znaor, A., Lortet-Tieulent, J., Laversanne, M., Jemal, A. & Bray, F. International variations and trends in renal cell carcinoma incidence and mortality. *Eur. urology* **67**, 519–530 (2015).
3. Kovacs, G. *et al.* The heidelberg classification of renal cell tumours. *The J. Pathol. A J. Pathol. Soc. Gt. Br. Irel.* **183**, 131–133 (1997).
4. Truong, L. D. & Shen, S. S. Immunohistochemical diagnosis of renal neoplasms. *Arch. pathology & laboratory medicine* **135**, 92–109 (2011).
5. Chen, F. *et al.* Multilevel genomics-based taxonomy of renal cell carcinoma. *Cell reports* **14**, 2476–2489 (2016).
6. Comprehensive molecular characterization of clear cell renal cell carcinoma. *Nature* **499**, 43 (2013).
7. Comprehensive molecular characterization of papillary renal-cell carcinoma. *New Engl. J. Medicine* **374**, 135–145 (2016).
8. Davis, C. F. *et al.* The somatic genomic landscape of chromophobe renal cell carcinoma. *Cancer cell* **26**, 319–330 (2014).
9. Bostwick, D. G. & Eble, J. N. Diagnosis and classification of renal cell carcinoma. *Urol. Clin. North Am.* **26**, 627–635 (1999).
10. Bonsib, S. M. Risk and prognosis in renal neoplasms: A pathologist's prospective. *Urol. Clin. North Am.* **26**, 643–660 (1999).
11. Soyer, P. *et al.* Renal cell carcinoma of clear type: correlation of ct features with tumor size, architectural patterns, and pathologic staging. *Eur. radiology* **7**, 224–229 (1997).
12. Amin, M. B. *et al.* Papillary (chromophil) renal cell carcinoma: histomorphologic characteristics and evaluation of conventional pathologic prognostic parameters in 62 cases. *The Am. journal surgical pathology* **21**, 621–635 (1997).
13. Delahunt, B. & Eble, J. N. Papillary renal cell carcinoma: a clinicopathologic and immunohistochemical study of 105 tumors. *Mod. pathology: an official journal United States Can. Acad. Pathol. Inc* **10**, 537–544 (1997).
14. Megumi, Y. & Nishimura, K. Chromophobe cell renal carcinoma. *Urol. internationalis* **61**, 172–174 (1998).
15. Zhang, J. *et al.* Solid renal cortical tumors: differentiation with ct. *Radiology* **244**, 494–504 (2007).
16. Sheir, K. Z., El-Azab, M., Mosbah, A., El-Baz, M. & Shaaban, A. A. Differentiation of renal cell carcinoma subtypes by multislice computerized tomography. *The journal urology* **174**, 451–455 (2005).
17. Kim, J. K. *et al.* Differentiation of subtypes of renal cell carcinoma on helical ct scans. *Am. J. Roentgenol.* **178**, 1499–1506 (2002).
18. Ruppert-Kohlmayr, A. J., Uggowitz, M., Meissnitzer, T. & Ruppert, G. Differentiation of renal clear cell carcinoma and renal papillary carcinoma using quantitative ct enhancement parameters. *Am. J. Roentgenol.* **183**, 1387–1391 (2004).
19. Young, J. R. *et al.* Clear cell renal cell carcinoma: discrimination from other renal cell carcinoma subtypes and oncocytoma at multiphasic multidetector ct. *Radiology* **267**, 444–453 (2013).
20. Djuric, U., Zadeh, G., Aldape, K. & Diamandis, P. Precision histology: how deep learning is poised to revitalize histomorphology for personalized cancer care. *NPJ precision oncology* **1**, 22 (2017).
21. Gutman, D. A. *et al.* Cancer digital slide archive: an informatics resource to support integrated in silico analysis of tcga pathology data. *J. Am. Med. Informatics Assoc.* **20**, 1091–1098 (2013).
22. Weinstein, J. N. *et al.* The cancer genome atlas pan-cancer analysis project. *Nat. genetics* **45**, 1113 (2013).
23. Cheng, J. *et al.* Integrative analysis of histopathological images and genomic data predicts clear cell renal cell carcinoma prognosis. *Cancer research* **77**, e91–e100 (2017).
24. He, K., Zhang, X., Ren, S. & Sun, J. Deep residual learning for image recognition. In *Proceedings of the IEEE conference on computer vision and pattern recognition*, 770–778 (2016).
25. Simonyan, K. & Zisserman, A. Very deep convolutional networks for large-scale image recognition. *arXiv preprint arXiv:1409.1556* (2014).
26. Russakovsky, O. *et al.* Imagenet large scale visual recognition challenge. *Int. J. Comput. Vis.* **115**, 211–252 (2015).
27. Girshick, R., Donahue, J., Darrell, T. & Malik, J. Rich feature hierarchies for accurate object detection and semantic segmentation. In *Proceedings of the IEEE conference on computer vision and pattern recognition*, 580–587 (2014).
28. Ren, S., He, K., Girshick, R. & Sun, J. Faster r-cnn: Towards real-time object detection with region proposal networks. In *Advances in neural information processing systems*, 91–99 (2015).
29. Ronneberger, O., Fischer, P. & Brox, T. U-net: Convolutional networks for biomedical image segmentation. In *International Conference on Medical image computing and computer-assisted intervention*, 234–241 (Springer, 2015).
30. Cruz-Roa, A. *et al.* Accurate and reproducible invasive breast cancer detection in whole-slide images: A deep learning approach for quantifying tumor extent. *Sci. reports* **7**, 46450 (2017).
31. Liu, Y. *et al.* Detecting cancer metastases on gigapixel pathology images. *arXiv preprint arXiv:1703.02442* (2017).
32. Han, Z. *et al.* Breast cancer multi-classification from histopathological images with structured deep learning model. *Sci. reports* **7**, 4172 (2017).
33. Coudray, N. *et al.* Classification and mutation prediction from non-small cell lung cancer histopathology images using deep learning. *Nat. medicine* **24**, 1559 (2018).
34. Wang, S. *et al.* Comprehensive analysis of lung cancer pathology images to discover tumor shape features that predict survival outcome. *Sci. reports* **7**, 10393 (2018).
35. Yu, K.-H. *et al.* Predicting non-small cell lung cancer prognosis by fully automated microscopic pathology image features. *Nat. communications* **7**, 12474 (2016).
36. Khosravi, P., Kazemi, E., Imielinski, M., Elemento, O. & Hajirasouli, I. Deep convolutional neural networks enable discrimination of heterogeneous digital pathology images. *EBioMedicine* **27**, 317–328 (2018).
37. del Toro, O. J. *et al.* Convolutional neural networks for an automatic classification of prostate tissue slides with high-grade gleason score. In *Medical Imaging 2017: Digital Pathology*, vol. 10140, 101400O (International Society for Optics and Photonics, 2017).
38. Agarwal, N., Balasubramanian, V. N. & Jawahar, C. V. Improving multiclass classification by deep networks using dagsvm and triplet loss. *Pattern Recognit. Lett.* **112**, 184–190 (2018).
39. Goyal, R., Gersbach, E., Yang, X. J. & Rohan, S. M. Differential diagnosis of renal tumors with clear cytoplasm: clinical relevance of renal tumor subclassification in the era of targeted therapies and personalized medicine. *Arch. pathology & laboratory medicine* **137**, 467–480 (2013).
40. Ricketts, C. J. *et al.* The cancer genome atlas comprehensive molecular characterization of renal cell carcinoma. *Cell reports* **23**, 313–326 (2018).
41. Lin, T.-Y. & Maji, S. Visualizing and understanding deep texture representations. In *Proceedings of the IEEE Conference on Computer Vision and Pattern Recognition*, 2791–2799 (2016).

42. Paszke, A. *et al.* Automatic differentiation in pytorch (2017).
43. Phoulady, H. A., Goldgof, D. B., Hall, L. O. & Mouton, P. R. Nucleus segmentation in histology images with hierarchical multilevel thresholding. In *Medical Imaging 2016: Digital Pathology*, vol. 9791, 979111 (International Society for Optics and Photonics, 2016).
44. R Core Team. *R: A Language and Environment for Statistical Computing*. R Foundation for Statistical Computing, Vienna, Austria (2014).
45. Therneau, T. M. *A Package for Survival Analysis in S* Version 2.38 (2015).

Author Contributions

S.T. developed the models for various tasks. S.T., P.K.V. and C.V.J. analyzed and discussed the data. S.T., P.K.V. and C.V.J. wrote the manuscript. P.K.V. and C.V.J. conceived the study and were in charge of overall direction and planning.

Additional Information

Supplementary information accompanies this paper at <https://doi.org/10.1038/s41598-019-46718-3>.

Competing Interests: The authors declare no competing interests.

Publisher's note: Springer Nature remains neutral with regard to jurisdictional claims in published maps and institutional affiliations.



Open Access This article is licensed under a Creative Commons Attribution 4.0 International License, which permits use, sharing, adaptation, distribution and reproduction in any medium or format, as long as you give appropriate credit to the original author(s) and the source, provide a link to the Creative Commons license, and indicate if changes were made. The images or other third party material in this article are included in the article's Creative Commons license, unless indicated otherwise in a credit line to the material. If material is not included in the article's Creative Commons license and your intended use is not permitted by statutory regulation or exceeds the permitted use, you will need to obtain permission directly from the copyright holder. To view a copy of this license, visit <http://creativecommons.org/licenses/by/4.0/>.

© The Author(s) 2019